Aerodynamic Performance Analysis of a Hypersonic Inlet Isolator Using Computation and Experiment

Birgit U. Reinartz,[*] Carsten D. Herrmann,[†] and Josef Ballmann[‡]
Aachen University, D-52056 Aachen, Germany
and
Wolfgang W. Koschel[§]
DLR, German Aerospace Research Center, D-74239 Hardthausen, Germany

A two-dimensional mixed compression inlet model with a subsequent isolator section is tested under Mach 4 and 5 flight conditions. Different configurations of the isolator are assessed with respect to their compression efficiency. The experimental investigations yield schlieren pictures of the isolator flow and static surface pressure measurements. The numerical simulations are performed with a Reynolds-averaged Navier–Stokes solver using a k–ω turbulence model, especially extended for modeling high-speed wall-bounded flows and separation regions. The close collaboration of experiment and simulation is beneficial: Validation of the simulation is achieved by the test data and the flowfield information available in the computational fluid dynamics results is employed to interpret the experimental findings and to compute the performance parameters. The computed static pressure ratios are in excellent agreement with empirical predictions. Furthermore, the investigations show that increasing the isolator length reduces the pressure sensitivity of the inlet. However, the experimental tests show that above a certain isolator length, no further increase of the sustainable backpressure is possible.

Nomenclature

A	=	area
h	=	isolator height
l	=	isolator length
M	=	Mach number
p	=	pressure
Re	=	Reynolds number
T	=	temperature
α	=	angle of attack
Δ	=	throttling degree
$\delta_1, \ldots, \delta_4$	=	intake geometry angle
η_C	=	adiabatic compression efficiency
η_{KE}	=	adiabatic kinetic energy efficiency
θ	=	momentum boundary layer thickness
π_C	=	total pressure recovery coefficient

Subscripts

back	=	outflow boundary of computational domain
e2	=	ejector 2
t	=	total condition
2	=	isolator entrance (station 2)
3	=	combustor/diffusor entrance (station 3)
$\infty, 0$	=	freestream conditions (station 0)

Introduction

T HE aerodynamic design of hypersonic inlets is a critical issue for the overall performance of an airbreathing propulsion system and is the subject of recent investigations.[1−4] The primary purpose of the inlet is to provide homogeneous high-pressure flow to the engine with a minimum of aerodynamic losses. Compression is performed through a series of oblique shock waves and internal contraction that lead to a shock wave/expansion wave interaction pattern inside the inlet. A schematic of the complex flowfield is shown in Fig. 1. A special feature of the scramjet inlet is that a large portion of the compression is achieved by an internal precombustion shock system.[5] The engine component responsible for this internal compression is the isolator, which protects the inlet from upstream disturbances of the high-pressure combustion zone. The developing shock train provides an elegant mechanism for supersonic flow to adjust to a specific backpressure. Whether a normal or an oblique shock train develops is mainly determined by the conditions at the isolator entrance, in particular Mach number and boundary-layer thickness.[6] Figure 2 shows a schematic of the normal shock train developing for entrance Mach numbers below $M_2 = 2 - 3$. Here, station 2 corresponds to the location where the turning of the external compression is completely canceled by the inlet geometry, and station 3 is the combustor entrance. The major portion of the compression is achieved by the first normal shock that separates the boundary layer. Afterward, the boundary-layer thickness increases rapidly and evens the pressure rise over the subsequent shock waves to a continuous compression. The maximum compression achievable by a shock train (neglecting viscous effects) is that of a normal shock wave, provided that the isolator is sufficiently long. If the backpressure exceeds this limit, the shock train is disgorged and the engine unstarts.

The performance of the inlet can be assessed in form of various parameters. Typical performance parameters are the mass flow ratio (MFR), the adiabatic kinetic energy efficiency η_{KE}, and the adiabatic compression efficiency η_C. The MFR denotes how much of the maximum possible amount of flow at freestream conditions through the inlet is being captured. When isentropic expansion is assumed, the adiabatic kinetic energy efficiency is the ratio of kinetic energy of the decelerated flow to the kinetic energy of the undisturbed flow. For an ideal gas, η_{KE} is a function of the total pressure recovery coefficient $\pi_C = p_{t,3}/p_{t,0}$ and the freestream Mach number.[6] Finally, the ratio of the isentropically achieved enthalpy increase over the actual increase of the compression process is denoted as compression efficiency, and in the adiabatic case, a relationship can be derived that states $\eta_c = f(\pi_C, M_\infty, M_3)$ (Ref. 6).

*Research Assistant, Mechanics Laboratory. Member AIAA.
†Research Assistant, Jet Propulsion Laboratory.
‡Professor, Mechanics Laboratory. Affiliate Member AIAA.
§Director, Institute for Space Propulsion. Senior Member AIAA.
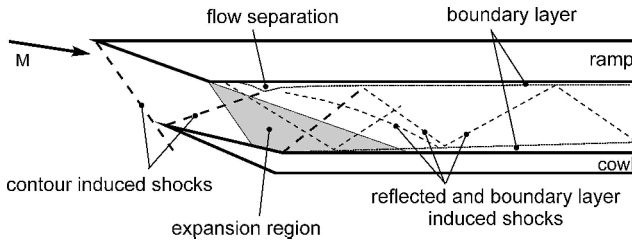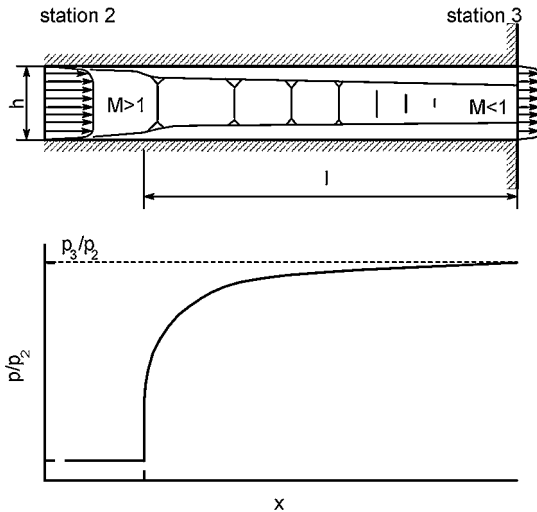
Fig. 1 Flow field schematic.

Fig. 2 Schematic of the flow pattern and wall pressure distribution of a normal shock train.[6]

The main focus of the present investigation is a parametric study of the isolator length at Mach numbers of $M_\infty = 2.5$ and 3.0, which correspond to flight Mach numbers of 4.1 and 5.3, respectively. In the experiment, eight different geometries are tested, and four of those geometries are also analyzed numerically. The experimental test data provide the necessary validation of the numerical simulations, which are needed to compute the performance parameters. Furthermore, the numerical simulations complete the knowledge of the flowfield in areas that are not accessible for measurements and, thus, are an important diagnostic to understand the test data.

Experimental Setup

Test Bed

The open-circuit wind tunnel at the Aachen Jet Propulsion Laboratory has been used in several inlet investigations.[7,8] The test bed is connected to a central compressor station, which supplies a continuous mass flow of 5.5 kg/s. The total temperature at the inlet of the test section ranges from 290 to 380 K and can be adjusted by use of a precooling system. Two separate Laval nozzles are used to realize the inlet Mach numbers $M_\infty = 2.5$ and 3.0. For the $M_\infty = 3.0$ measurements, the nozzle has to be connected to a low-pressure chamber to establish the necessary pressure ratio for the expansion to accelerate the inlet velocity. The low-pressure chamber is evacuated by a variable ejector system. A second ejector system is connected to the inlet model for the evacuation of the inner flow. For the simulation of different throttling conditions, the second ejector can be adjusted during the test. To compare the throttling conditions of the different model configurations, a throttling degree Δ is defined using the ratio of the ejector entrance area and the model exit area:

$$\Delta = (1 - A_{e2}/A_{exit}) \cdot 100 \tag{1}$$

According to Eq. (1), the throttling degree can be varied between $\Delta = 0\%$ (fully opened) and 100% (fully closed).

The side walls of the low-pressure chamber and the inlet model are equipped with glass windows to obtain optical access. The test bed is shown in Fig. 3.

Table 1 Main dimensions of the inlet model

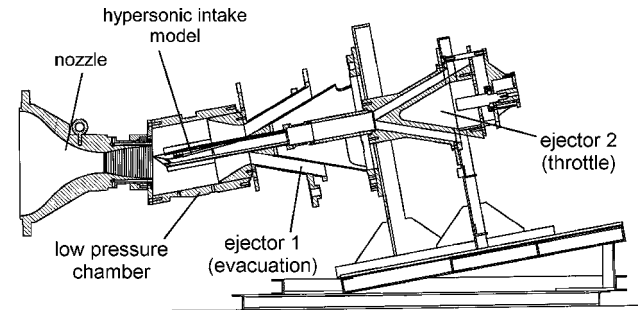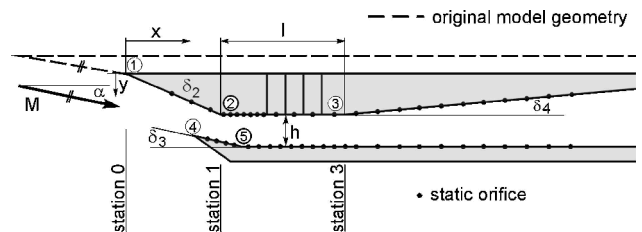| Quantity	Value
Inner width	52 mm
Overall length	400 mm
Isolator height h	15 mm
Second ramp angle δ_2	21.5 deg
Cowl angle δ_3	9.5 deg
Divergence angle δ_4	5 deg

Fig. 3 Inlet model test bed.

Fig. 4 Main dimensions of the model.

Inlet Models

The subject of the present study is the influence of the isolator length variation on the inlet performance. The overall inlet geometry is based on similar inlet models tested within the frame of earlier German research activities.[9,10] The design with respect to the external ramp angles and the position of the engine cowl was the focus of a research project[7,11] preceding the current work. In that project, a fixed geometry for the external compression was chosen considering start behavior of the inlet and minimizing ramp flow separation. In this original model geometry (dashed line in Fig. 4), two consecutive ramps deflect the flow before entering the inlet with subsequent interior compression. However, because of the restrictions of the wind tunnel used, the experimental setup requires that the first outer compression ramp of the inlet geometry be omitted in the current experimental testing to attain the specified test conditions for the isolator study. As shown in Fig. 4, the given angle of attack of the freestream, $\alpha = -10$ deg, arises from the missing first ramp. The design Mach number of the second ramp is $M_\infty = 3.0$.

The outline of the inlet contour and the definition of the main dimensions are given in Fig. 4 and in Table 1. The design of the model allows the variation of the isolator length l within the range of 29.3–99.3 mm by inserting additional pieces (width of 10 mm).

Because of a serious flow separation on the inlet ramp at $M_\infty = 3.0$, it was assumed that the boundary layer is still transitional at the point of separation. Therefore, a turbulence producing wire (∅ = 0.9 mm) was mounted at the ramp at $x = 40$ mm to ensure a fully turbulent boundary layer.

Data Recording

The investigated subscale inlet model is a two-dimensional configuration with a width-to-height ratio of 3.5. To obtain detailed information on the internal shock pattern and shock/boundary layer-interactions, a two-dimensional, color-schlieren system has been installed at the test facility. Because of the integrating effect of
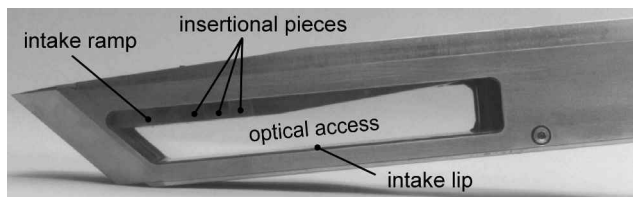
Fig. 5   Inlet model.

the schlieren technique, it is assumed that the influence of three-dimensional flow effects, such as the effect of side wall compression, on the schlieren pictures is neglectable in comparison to the two-dimensional main flow.

A xenon lamp lightened color mask with separate color fields is used as the schlieren light source. The color fields of the mask are adapted to the desired density gradients and to the applied light source to obtain colored regions of equal brightness and extension, as well as a suitable definition of the model contour.[12] For the separation of the schlieren colors, a slit diaphragm is used as schlieren edge in the focus of the concave mirror of the picture side. The schlieren pictures are taken by use of a digital camera, which is directly connected to the measurement computer. Because of the resolution of the digital camera and the high width-to-length ratio of the model window (Fig. 5), the schlieren pictures of the inlet flow are built up of two overlapping frames.

For additional information about the flowfield, the wall pressure distributions along the model centerline are measured. The positions of the wall pressure holes can be taken from Fig. 4. Because of the sequential measurement mode, the pressure distributions can only be evaluated for stationary conditions. A detailed overview of the obtained test data is given by Herrmann and Koschel.[13]

Numerical Method

Navier–Stokes Solver FLOWer

The computations are performed with the FLOWer code[14,15] including some extensions for hypersonic flows.[16] The code uses a finite volume technique with upwind discretization on block-structured grids to solve the unsteady three-dimensional compressible Reynolds-averaged Navier–Stokes equations. Because of the moderate test conditions, for example, $T_{t,0} \approx 300$ K, during the wind-tunnel experiment, the air is considered to be a calorically perfect gas with constant ratio of specific heats, $\gamma = 1.4$. The computational domain is divided into nonoverlapping hexahedra in general curvilinear coordinates, and the spatial discretization is performed by a cell-centered formulation. To account for the directed propagation of information in the inviscid part of the equations, the advection upstream splitting method (AUSM) flux vector splitting is applied for the approximation of the convective flux functions.[17] Higher-order accuracy for the upwind discretization and consistency with the central differences used for the diffusive terms is achieved by the monotonic upstream scheme for conservation laws extrapolation, and the total variation diminishing property of the scheme is ensured by either a modified van Albada[18] or a van Leer[19] limiter function. Time integration is performed by an explicit five-stage Runge–Kutta time-stepping scheme. To enhance convergence, a multigrid method, implicit residual smoothing, and local time stepping are applied.

Turbulence Model

Because of the high Reynolds number of approximately 5×10^7/m achieved in the hypersonic test bed, turbulent flow is assumed for the numerical simulations. A small freestream turbulence intensity Tu_∞ of 0.5% is specified because the simulation of the transition process is not yet implemented in the code. All flow computations are performed with a compressible low Reynolds number k–ω model[20] with some extensions for modeling high-speed wall bounded flows and separation regions.[17] The spatial discretization is performed using an AUSM upwind scheme for the convective and central discretization for the diffusive terms. The low Reynolds

Table 2   Test conditions for supersonic inlet

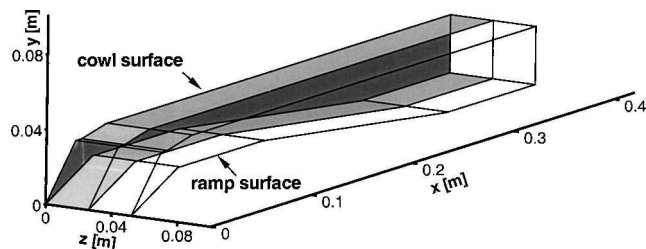| M_∞	$Re_{x\infty}$ [1/m]	$p_{t,0}$, kPa	$T_{t,0}$, K
2.41	5.07×10^7	540	305
3.0	4.87×10^7	620	290

Fig. 6   Numerical representation of one-half of the three-dimensional test model with swept side walls.

number damping terms as well as the high grid aspect ratios near the wall make the system of turbulence model equations stiff. To increase the numerical stability of turbulent flow simulations, the time integration of the turbulence equations is decoupled from the mean flow equations, and the turbulence equations are solved using a diagonal dominant alternating direction implicit scheme.[21]

Boundary Conditions

The supersonic inflow is defined by specifying the flow conditions at the inlet of the test section given in Table 2. The turbulent values are determined by the specified freestream turbulence intensity: $k_\infty = 1.5(Tu_\infty u_\infty)^2$ and $\omega_\infty = k_\infty/(0.001 \cdot \mu)$. In case of predominant supersonic outflow, the variables are completely extrapolated from the interior onto the boundary. Otherwise, the influence of the throttle is simulated with a prescribed backpressure ratio, p_{back}/p_0, at the outflow boundary, and the remaining variables are extrapolated. At solid walls, the no-slip condition is enforced by setting the velocity components to zero. Additionally, the turbulent kinetic energy and the normal pressure gradient are set to zero. The specific dissipation rate is set proportional to the wall shear stress and the surface roughness.[22] Because the total temperature of the flow is in the range of ambient temperature and because of the long measuring times of 30 min or more, the surface temperature of the test model is assumed to approach the adiabatic wall temperature. The adiabatic energy boundary condition is directly applied by zeroing the contributions of the wall faces to the dissipative fluxes. Reconstruction at boundary nodes is accomplished employing ghost cells, which allow for a similar treatment of all physical cells and minimize the computational effort for the boundary conditions. At the symmetry plane of the half-configuration, the conservation variables are mirrored onto the ghost cells to ensure symmetry.

Computations

The design of the experiment assumed a predominantly two-dimensional flow behavior where measurements were only taken in the center plane. To assess the possible influence of the swept side walls on the flow in the center plane, a three-dimensional numerical simulation of one-half of the inlet model (Fig. 6) was performed. Comparison of the wall pressure distributions for the unthrottled case in Fig. 7 yields the flow in the symmetry plane to be almost identical to corresponding two-dimensional simulations. This analysis assured that the entrance condition into the isolator symmetry plane are not influenced by three-dimensional effects. To save on computational time, the three-dimensional computation was not continued for the pressurized flow conditions, neglecting the possible effect of separation on the isolator side walls on the developing shock train in the center plane. Instead, a two-dimensional analysis of the flowfield was initiated. The applied two-dimensional representation of the inlet model with mathematically sharp leading edges for the ramp and the engine cowl is shown in Fig. 8.
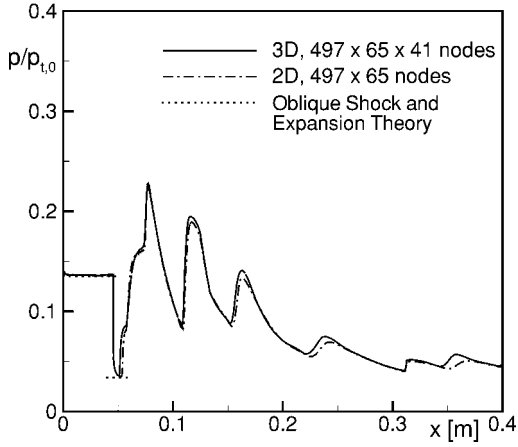
Fig. 7 Computed wall pressure distribution along the compression ramp surface and in the symmetry plane.
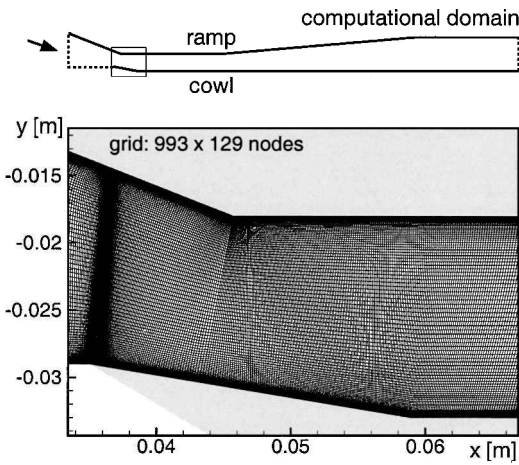

Fig. 8 Computational domain and grid detail for supersonic inlet.

Fig. 9 Residual for supersonic inlet computation.

Fig. 10 Surface pressure distribution for refined grids.

The computations are performed on a SunFire shared memory processors (SMP)-cluster using up to 26 processors as well as on a NEC SX-5 cluster. The parallelization is jointly based on FLOWer's block-based message passing interface formulation[23] as well as on Sun's shared-memory autoparallelization. A Courant–Friedrichs–Lewy number of 4 is realized, and the CPU time required for a turbulent flow simulation is approximately 8 h.

Numerical Accuracy

A complete validation of the FLOWer code has been performed before its release,[14,15,24] and continued validation is achieved by the analyses documented in subsequent publications.[11,16,17,22,25] The accuracy of the current investigation is evaluated by comparison with the experimental results. In addition, for the flow region from the inflow up to the expansion fan in Fig. 1, the oblique shock and expansion theory verifies the computed flow conditions (Fig. 7).

To ensure convergence of the numerical solution, the density residual and the turbulence residual ($L2$-norm) are monitored in Fig. 9. The solution can be considered as converged after approximately 15000 iterations for the two-level grid. At that stage, the density residual reaches its minimum value after falling for over four orders of magnitude. The turbulence residual behavior is less monotonic, but it drops five orders of magnitude. An additional convergence criterion enforced in the current analysis requires the difference between computed inflow and outflow mass flux to drop below 1%.

Grid Analysis

The performance of a grid sensitivity analysis confirmed that the grid resolution used in this study is sufficient to capture the phys-
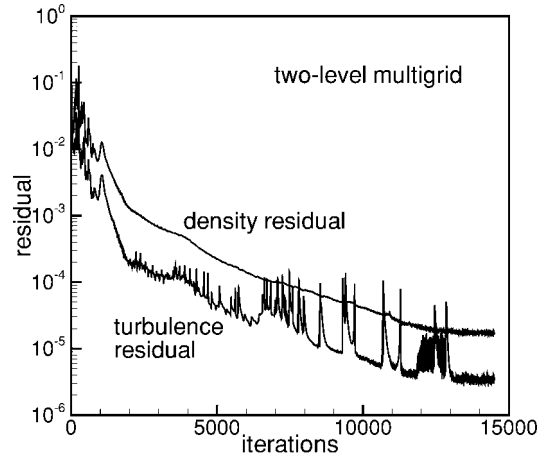
ically relevant features. In Fig. 10, the static pressure distribution along the cowl and the ramp surfaces are shown for three different grid-refinement levels: coarse (497×65), medium (993×129), and fine (1985×257). Out of this analysis, the medium grid was selected, and all results shown are computed applying this resolution with a minimum spacings of 1 μm in x and y directions. To ensure the accuracy of the turbulent flow solution, a value of y^+ below 1 is realized for the main portion of the wall flow region with a maximum of $y^+ = 2$ near the cowl deflection shock.

Results

The detailed results of the supersonic inlet are first presented for one geometry to outline the characteristics of unthrottled and of pressurized flow. In this context, the problem of modeling the transitional behavior of the boundary layer is discussed. Then the findings for the variation of isolator length and the obtained aerodynamic parameters of the inlet configurations are presented.

Supersonic Inlet Flow

The flowfield of the unthrottled supersonic inlet at $M_\infty = 2.41$ and for an isolator length of $l = 79.3$ mm is presented in Fig. 11. The flow expands around the edge of the compression ramp corner, seen as dark colored region in the schlieren picture. Slightly downstream, the impingement of the lip shock on the ramp induces a small separation of the boundary layer. The corresponding separation and reattachment shock are visible as two lines divided by another dark-colored expansion. A further primary shock, which is induced by the cowl deflection angle, crosses the separation and reattachment shocks, is reflected at the ramp, and impinges at almost the same
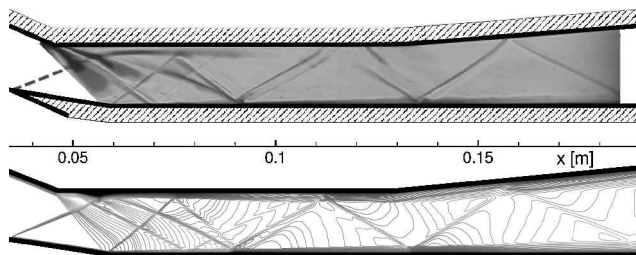
Fig. 11   Comparison of a schlieren picture (top) without throttling and corresponding Mach number contour lines (bottom) of the computation; $M_\infty = 2.41$ and $l = 79.3$ mm.
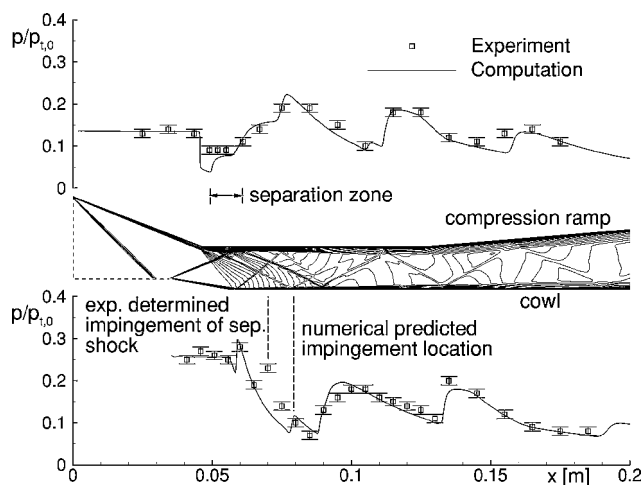

Fig. 12   Mach contours (computed) and surface pressure distribution without throttling; $M_\infty = 2.41$ and $l = 79.3$ mm.

location as the reattachment shock on the cowl surface. Downstream, the repeatedly reflected shocks visibly weaken. Comparison of the schlieren picture with the likewise presented Mach number contours of the computation reveals an overall good agreement. The shock wave pattern, the separation, and the approximate boundary-layer thickness of the schlieren picture are also present in the simulation. The surface pressure distributions, shown in Fig. 12, allow for a more quantitative comparison between numerical and experimental results. Here, a discrepancy in the ramp pressure distribution can be seen in the expansion region with subsequent separation. The computed separation appears smaller than experimentally observed, and thus, the separation shock is weaker and impinges downstream of the measured location on the cowl surface. The reason for the discrepancy is probably a deficiency of the turbulence model to predict transitional behavior in the flow. Because of the expansion, the boundary layer is laminarized, as will be discussed in more detail in the following section, and the turbulence model is not able to predict the changing state of the boundary layer correctly. Otherwise, the computed pressure distributions for the compression ramp, as well as the cowl surface, compare favorably with the experimentally obtained pressure measurements. The discrepancy between measurements and simulation in the diffuser section is due to the grid resolution in this section, which is reduced for the benefit of a better resolution in the inlet and isolator. Overall, the agreement between simulation and experiment is favorable.

Transitional Behavior

During the inlet experiments for the second Mach number, $M_\infty = 3.0$, a severe separation of the ramp boundary layer appeared that covered about one-third of the isolator height (Fig. 13). For an inlet, a separation of this size is not tolerable due to the flow blockage and the resulting unsteadiness of the flow. Therefore, a wire was mounted on the ramp to increase the turbulence level of the boundary layer and to make it more resistant to adverse pressure gradients. This technique proved successful as is shown in Fig. 14. However,
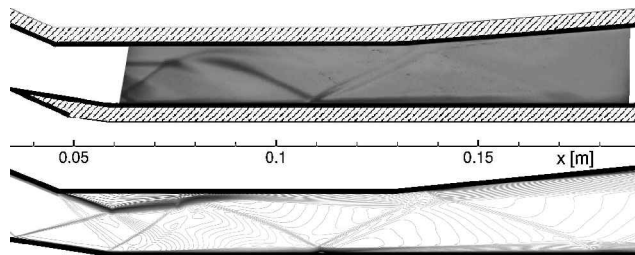

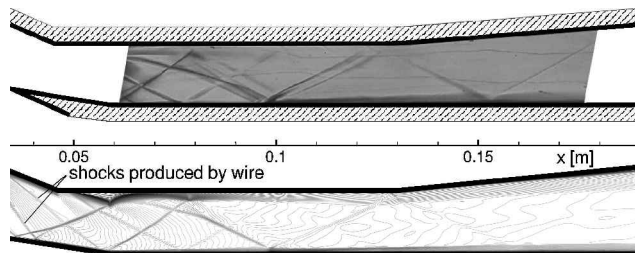**Fig. 13   Large separation occurring after boundary layer is laminarized due to strong expansion.**

Fig. 14   Size of separation is greatly reduced by insertion of a turbulence producing wire in the flow.
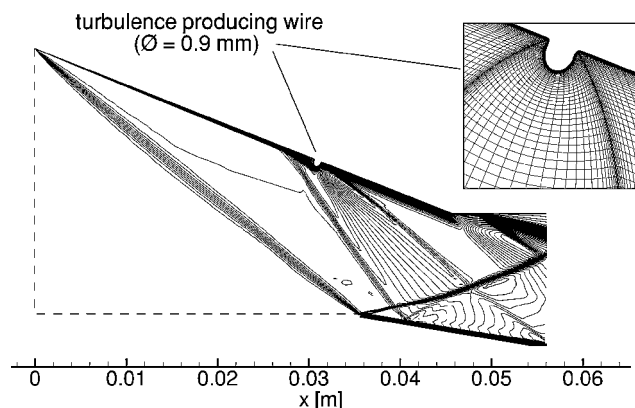

Fig. 15   Flowfield and grid detail in the vicinity of the mounted wire.

a numerical simulation was initiated to better understand the reasons and to visualize the flow pattern not visually accessible in the experiments. Therefore, the disturbance introduced by the wire was simulated with great care. Figure 15 shows the grid, as well as the flowfield in the vicinity of the wire. Prandtl–Meyer expansion theory yields that the expansion of the $M_\infty = 3.0$ flow is 1.3 times stronger than the respective expansion at $M_\infty = 2.41$. The subsequent computations of the inlet flow with and without the wire showed that the expansion is indeed strong enough to change the state of the boundary-layer flow. Even though, the turbulence model is not able to predict transition, the turbulence intensity reduced enough during the expansion that a separation of comparable size was determined for the wireless case (Fig. 13). In Fig. 14, the flow pattern obtained for the simulation including the wire is shown, yielding two additional induced shock waves (also see Fig. 15). Downstream of the wire, the boundary-layer thickness is visibly increased, and the vorticity level is raised whereby the separation is greatly reduced. In Fig. 14, the concurrence of the shock wave locations between the schlieren picture and Mach number contours is very satisfactory. The computations fully explain the altered schlieren wave pattern between the two experimental setups.

Pressurized Isolator Flow

In hypersonic engines, a precombustion shock system develops inside the isolator because of the subsequent high-pressure combustion zone. To produce a similar shock wave pattern in the
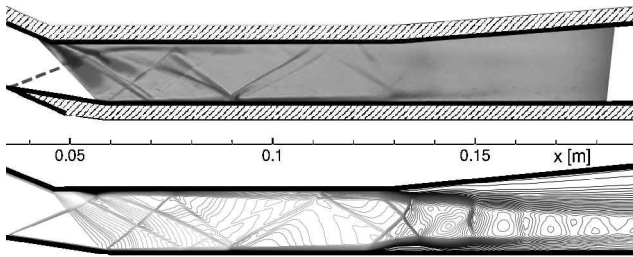
Fig. 16   Comparison of a schlieren picture with $\Delta = 70\%$ and corresponding Mach number contour lines with a specified backpressure ratio of 7.
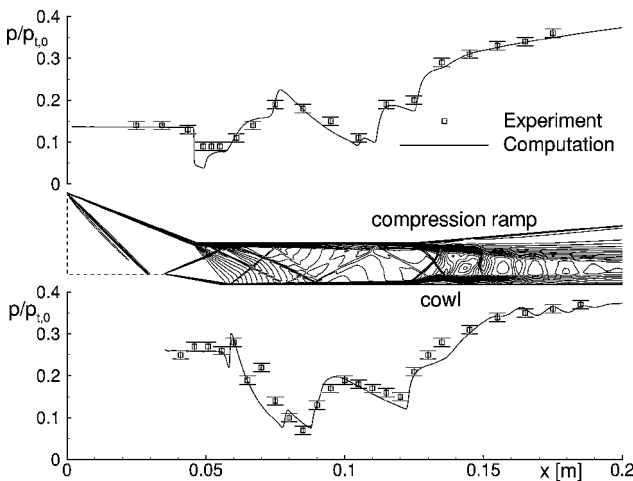

Fig. 17   Mach contours (computed) and surface pressure distribution for $\Delta = 70\%$ and $p_{back}/p_0 = 7$.

Fig. 18   Surface pressure distribution for different throttling degrees Δ and backpressure ratios.

Fig. 19   Computed normal shock train in the isolator; $M_\infty = 2.41$ and $p_{back}/p_0 = 8.25$.

single-engine-component testing, throttling is applied to the flow. In the computations, the effect of the operating engine is simulated by a specified backpressure ratio. Because there exists no mathematical dependence between the throttling degree Δ and the backpressure ratio, the achieved pressure buildup in the isolator is compared to obtain a correlation. Figure 16 shows the flow pattern for an operating point of $\Delta = 70\%$ and the corresponding simulation with $p_{back}/p_0 = 7$. The flow remains supersonic until it reaches the diffusor section. Consequently, the complex shock wave/expansion wave interaction pattern in the isolator remains the same as described earlier. Inside the diffusor, an incipient shock train is detectable. The high backpressure leads to the separation of the upper and lower boundary layer and generates a shock wave pattern of two crossing oblique shock waves. Because of the constriction of the main flow, especially on the ramp side, the flow accelerates again and enters the subsonic regime with a normal shock. Afterward, the flow remains subsonic and slowly becomes more homogeneous. The separation of the boundary layer is also visible in the schlieren picture; however, the shock structure can only be anticipated and has to be deduced from the simulation. In Fig. 17, the pressure buildup proceeds continuously due to the rapidly growing boundary layers. Some small wiggles can be seen in the computed cowl surface pressure distribution, indicating the alternately decelerating and accelerating flow. As the degree of throttling is increased, the onset of pressure buildup moves upstream into the isolator. Figure 18 shows ramp surface pressure distributions for different throttling degrees and corresponding backpressure ratios. At $\Delta = 73\%$ ($p_{back}/p_0 = 8.25$), the complete isolator contributes to the pressure buildup, and the maximum pressure ratio p_3/p_2 attainable for this configuration is achieved. After only a slight shift of the operating point ($\Delta = 74\%$ and $p_{back}/p_0 = 8.5$), the complete ramp boundary layer separates up to the expansion region. A further increase of the throttling degree causes a severe flow blockage and leads to a strong decrease in captured mass flow. At this condition, the inlet is no longer started.
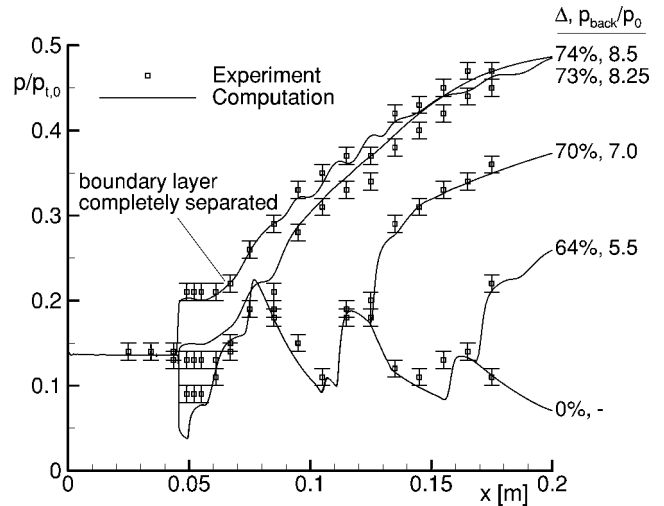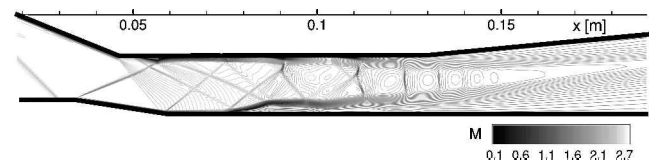
The flowfield of a fully developed normal shock train is presented in Fig. 19. Because of the nonhomogenous flow entering the isolator, the actual shock train starts at an approximate axial position of $x = 0.11$ m. Upstream of this position, the corresponding pressure distribution in Fig. 18 reveals a compression/expansion interaction pattern typical for reflected oblique shock waves but no continuous pressure buildup inherent in a shock train. At $x = 0.11$ m, an initial normal shock immediately following two crossing oblique shock waves and marking the onset of the shock train can be seen in Fig. 19. The primary shock is followed by two secondary normal shock waves in the main flow, which is increasingly constricted by the growing boundary layers. The pressure distribution in Fig. 18 shows that the majority of the pressure increase is achieved with the initial normal shock. The far weaker secondary shocks cause the pressure to rise only gradually.
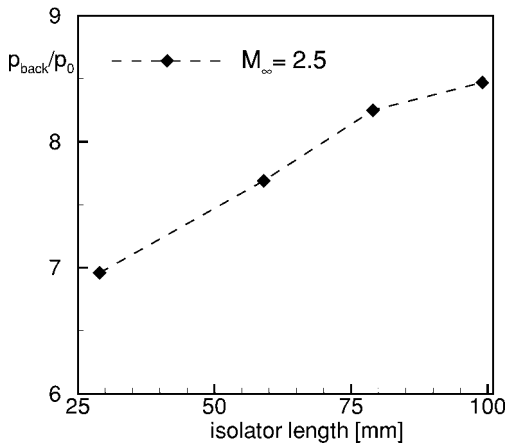
Isolator Length Variation

The results presented in the preceding section illustrate that the compression achievable by the isolator is limited by its length. However, the rapidly growing boundary layers induce viscous losses that may erase the benefit of an additional length increase, and the theoretical goal of a normal shock compression ratio cannot be attained. During the experimental testing, eight isolator geometries of different length were analyzed, and four of the geometries are also studied numerically.

Figure 20 shows the ability of the different isolator configurations to protect the inlet against the pressure disturbances of the succeeding components. In the experimentally determined diagram (Fig. 20a), the maximum allowable throttling degree,[13] for which a complete separation of the ramp boundary layer is avoided (Fig. 18), is plotted against the isolator length. It can be seen that up to a certain amount an increase of the isolator length leads to a decrease of the pressure sensitivity of the inlet. However, a further extension of the duct seems to have no additional impact. The computations yield a continuous growth of the sustainable backpressure with isolator length, starting from a pressure ratio of $p_{back}/p_0 = 6.9$ for the shortest duct ($l = 29$ mm) to $p_{back}/p_0 = 8.5$ for the longest analyzed isolator ($l = 99$ mm).
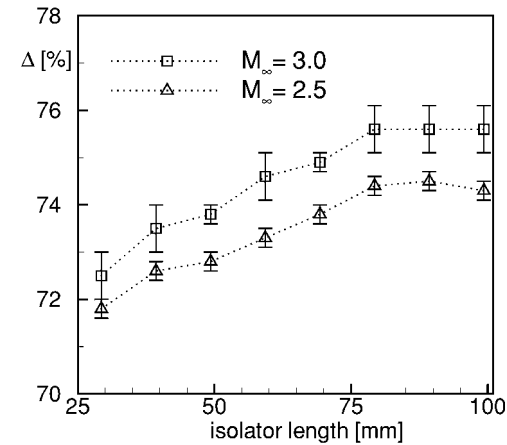
a) Experiment

b) Computation

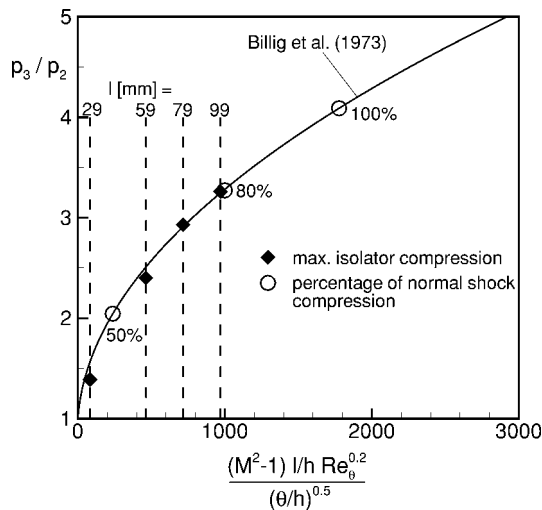**Fig. 20   Sustainable pressure ratios for different isolator lengths.**

Fig. 21   Empirical correlation for isolator length[26] and computed maximum compression ratios.

The maximum compression ratios obtained in the simulations are shown in Fig. 21. The well-known correlation by Waltrup and Billig[26] has been manipulated to yield the pressure ratio of a rectangular area isolator.[6,27] This correlation relates the attainable pressure ratio p_3/p_2 to the basic physical parameters such as the geometry (l and h), the Mach and Reynolds number at the isolator entrance, and the momentum boundary-layer thickness θ, where θ is an estimate for the additional area reduction caused by the inlet boundary layer. The maximum compression ratio is obtained when the com-

Table 3   Total pressure ratios

l, mm	$p_{t,2}/p_{t,0}$	$p_{t,3}/p_{t,2}$	π_C
29.3	0.917	0.867	0.795
59.3	0.917	0.712	0.653
79.3	0.917	0.692	0.635
99.3	0.917	0.690	0.632

Table 4   Performance parameters

l, mm	MFR	M_3	η_C	η_{KE}
29.3	0.905	1.52	0.477	0.942
59.3	0.904	0.90	0.849	0.889
79.3	0.905	0.73	0.855	0.881
99.3	0.906	0.61	0.862	0.879

plete isolator contributes to the pressure buildup. The agreement between the computed values and the pressure ratios predicted by the correlation is encouraging. Also note that the three longest selected geometries fall in a preferable design range. As indicated by the slope of the correlation curve, the pressure gain for a slight length increase in a short isolator is much larger than for a longer isolator. Therefore, the accompanying weight increase and the viscous losses may remedy the additional pressure gain for extremely long isolators, and the geometries are often designed to achieve 80% or even only 50% of the normal shock compression.[27]

The total pressure ratios and the adiabatic efficiency parameters of the inlet obtained from the numerical simulation are specified in Tables 3 and 4, respectively. In correspondence to the experiments, the different geometries are denoted by the length of the constant area duct l. However, a position $x = 0.0681$ m was chosen as isolator entrance (station 2), which is downstream of the reattachment of the ramp boundary layer, reducing the actual isolator length used for the parameter calculation. The values are obtained by either integration (mass flow) or averaging, for example, pressure, the distribution of the respective variable at the indicated stations. The total pressure recovery of the inlet section is not influenced by the isolator variation, and a value of 91.7% is obtained. The overall pressure recovery coefficient π_C of the shortest geometry ($l = 29$ mm) is extremely high with 0.795 because there is almost no isolator section. For the remaining configurations, π_C decreases from 0.653 to 0.623 with increasing length as the strength of the shocks present in the isolator shock train increases.

Because the MFR is determined by the inlet alone and is not a function of the isolator length, the slight variations in Table 4 are caused by the numerics. Because of the displacement effect of the boundary layers, the computed values lie slightly below the theoretical value of MFR $= 0.931$. Also specified are the averaged Mach numbers at the isolator exit, which are needed to calculate the compression efficiency. For the first configuration, an adiabatic compression efficiency η_C of less than 50% is achieved, whereas the adiabatic kinetic energy efficiency shows a high value of 94.2%. As shown in Fig. 21, there is almost no compression achieved within the shortest isolator; therefore, the flow is only slightly decelerated in the isolator section, keeping the kinetic energy at a high level and limiting the compression efficiency. This configuration is only a valid option if almost no internal compression is needed. The remaining configurations obtain a compression efficiency of about 85–86% and a kinetic energy efficiency of 88–89%, depending on their length. This confirms the interpretation of Fig. 21 that all three geometries might be a favorable choice for an isolator, depending on the requirements of the propulsion system.

Conclusions

The investigation of the present isolator configurations is motivated by the need for design methods of hypersonic inlets. On the one hand, experimental investigations of hypersonic flows are limited by the conditions attainable by the applied test bed and not all phenomena of high-speed flows can be modeled simultaneously.

On the other hand, computational tools have to be thoroughly validated using experimental data. Therefore, the current joint research project, containing numerical as well as experimental analysis, was initiated.

The main focus of the study is the variation of the isolator geometry and its influence on the overall inlet compression efficiency. For the investigation, eight isolator geometries of different lengths have been tested experimentally, and four of the geometries have been analyzed numerically to determine further performance parameters. The performance analysis yields that the first geometry, with an extremely short isolator section, is an unfavorable choice because there is almost no pressure gain achieved in the isolator. An adiabatic compression efficiency of about 85–86% and an adiabatic kinetic energy efficiency of 88–89% was achieved for the remaining inlet/isolator configurations. The obtained static pressure ratios are in excellent agreement with the empirical predictions. Furthermore, the investigations show that the sustainable backpressure is strongly influenced by the isolator length. Namely, increasing the isolator length reduces the pressure sensitivity of the inlet. However, the experimental tests showed that above a certain isolator length no further increase of the sustainable backpressure was possible.

A joint experimental and computational study is carried out, and the two techniques complement each other favorably. The available measurement data ensure the accuracy of the computed results and the information contained in the computational fluid dynamics (CFD) analysis supports the interpretation of the test data by completing the flowfield in areas that are not accessible to measurements. Modeling the transitional behavior of the inlet boundary layer, which alternately is subject to adverse and favorable pressure gradients, is still a deficiency of the numerical simulation. In this respect, the applied turbulence model, already specifically tuned to high-speed wall-bounded inlet flows, needs further improvement. The good agreement between experiment and CFD validate the applied computational tool for two-dimensional simulations of hypersonic inlet flows.

Acknowledgments

References

[1]Kanda, T., Tani, K., Kobayashi, K., Saito, T., and Sunami, T., "Mach 8 Testing of a Scramjet Engine with Ramp Compression," *Journal of Propulsion and Power*, Vol. 18, No. 2, 2002, pp. 417–423.

[2]Borisov, A. V., Bedarev, I. A., Fedorova, N. N., Nestulya, R. V., and Starov, A. V., "Numerical and Experimental Investigation of Supersonic Turbulent Flows in Plane Channels of Variable Cross-Section," *Proceedings of the International Conference on Methods of Aerophysical Research*, Russian Academy of Sciences, Novosibirsk, Russia, 2002, pp. 31–35.

[3]Watanabe, Y., Murakami, A., and Fujiwara, H., "Effect of Sidewall Configurations on the Aerodynamic Performance of Supersonic Air-Intake," AIAA Paper 2002-3777, July 2002.

[4]Bourdeau, C., Blaize, M., and Knight, D., "Performance Analysis for High-Speed Missile Inlets," *Journal of Propulsion and Power*, Vol. 16, No. 6, 2000, pp. 1125–1131.

[5]Van Wie, D. M., "Scramjet Inlets," *Scramjet Propulsion*, edited by E. T. Curran and S. N. B. Murthy, Vol. 189, Progress in Astronautics and Aeronautics, AIAA, Reston, VA, 2000, pp. 447–511.

[6]Heiser, W. H., and Pratt, D. T., "Compression Systems or Components," *Hypersonic Airbreathing Propulsion*, Educational Series, AIAA, Washington, DC, 1994, pp. 197–275.

[7]Schneider, A., and Koschel, W. W., "Detailed Analysis of a Mixed Compression Hypersonic Intake," International Society for Air Breathing Engines, Paper ISABE-99-7036, Sept. 1999.

[8]Koschel, W., Rick, W., and Rüggeberg, T., "Study of Flow Phenomena in High-Speed Intakes," AIAA Paper 92-5029, Nov. 1992.

[9]Schmitz, M. C., and Bissinger, N. C., "Design and Testing of a 2-D fixed Geometry Hypersonic Intake," AIAA Paper 98-1529, April 1998.

[10]Walther, R., Koschel, W., Sabelnikov, V., Korontsvit, Y., and Ivanov, V., "Investigations into the Aerothermodynamic Characteristics of Scramjet Components," International Society for Air Breathing Engines, Paper ISABE-97-7085, Sept. 1997.

[11]van Keuk, J., Ballmann, J., Schneider, A., and Koschel, W., "Numerical Simulation of Hypersonic Inlet Flows," AIAA Paper 98-1526, April 1998.

[12]Kleine, H., and Grönig, H., "Color Schlieren Methods in Shock Wave Research," *Shock Waves*, Vol. 1, No. 1, 1991, pp. 51–63.

[13]Herrmann, C. D., and Koschel, W. W., "Experimental Investigation of the Internal Compression of a Hypersonic Intake," AIAA Paper 2002-4130, July 2002.

[14]Kroll, N., Rossow, C.-C., Becker, K., and Thiele, F., "The MEGAFLOW Project," *Aerospace Science and Technology*, Vol. 4, No. 4, 2000, pp. 223–237.

[15]Radespiel, R., Rossow, C., and Swanson, R., "Efficient Cell-Vertex Multigrid Scheme for the Three-Dimensional Navier–Stokes Equations," *AIAA Journal*, Vol. 28, No. 8, 1990, pp. 1464–1472.

[16]Reinartz, B. U., van Keuk, J., Coratekin, T., and Ballmann, J., "Computation of Wall Heat Fluxes in Hypersonic Inlet Flows," AIAA Paper 2002-0506, Jan. 2002.

[17]Coratekin, T. A., van Keuk, J., and Ballmann, AIAA Paper 2001-1752, April 2001.

[18]van Albada, G. D., van Leer, B., and Roberts, W. W., "A Comparative Study of Computational Methods in Cosmic Gas Dynamics," *Astronomy and Astrophysics*, Vol. 108, 1982, pp. 76–84.

[19]van Leer, B., "Towards the Ultimate Conservative Difference Scheme V, A Second Order Sequel to Gudonov's Method," *Journal of Computational Physics*, Vol. 32, 1979, pp. 101–136.

[20]Wilcox, D. C., "Turbulence Energy Equation Models," *Turbulence Modeling for CFD*, 2nd ed., Vol. 1, DCW Industries, Inc., Palm Drive, CA, 1994, pp. 73–170.

[21]Bardina, J. E., Huang, P. G., and Coakley, T. J., "Turbulence Modeling Validation, Testing, and Development," NASA TM 110446, April 1997.

[22]Coratekin, T. A., "Numerical Simulation of Turbulent Shock/Boundary-Layer Interactions in Hypersonic Flows," *Strömungstechnik*, Vol. 7/381, Fortschritt-Berichte, Verein Deutscher Ingenieure, Düsseldorf, Germany, 2000, pp. 1–96.

[23]Aumann, P., Barnewitz, H., Schwarten, H., Becker, K., Heinrich, R., Roll, B., Galle, M., Kroll, N., Gerhold, Th., Schwamborn, D., and Franke, M., "MEGAFLOW: Parallel Complete Aircraft CFD," *Parallel Computing*, Vol. 27, May 2001, pp. 415–440.

[24]Becker, N., Kroll, N., Rossow, C. C., and Thiele, F., "Numerical Flow Calculations for Complete Aircraft—the Megaflow Project, *DGLR Jahrbuch 1998*, Vol. 1, Deutsche Gesellschaft für Luft- und Raumfahrt, Bonn, 1998, pp. 355–364.

[25]Reinartz, B. U., and Ballmann, J., "Details on the Computation of Hypersonic Inlet Flows," *Proceedings of GAMM Annual Meeting*, Vol. 1, Wiley, Weinheim, Germany, 2002, pp. 326, 327.

[26]Waltrup, P. J., and Billig, F. S., "Prediction of Precombustion Wall Pressure Distribution in Scramjet Engines," *Journal of Spacecraft and Rockets*, Vol. 10, No. 9, 1973, pp. 620–622.

[27]Koschel, W. W., "Scramjet Performance Calculation and Testing," *High Speed Propulsion*, edited by S. N. B. Murthy, Vol. 1, VKI Lecture Series, von Kármán Insitute, Waterloo, Belgium, 1998, pp. 7.1–7.35.